Materials Advances

ROYAL SOCIETY OF CHEMISTRY

PAPER

View Article Online
View Journal | View Issue

Check for updates

Cite this: *Mater. Adv.*, 2026, 7, 3177

Quasi-isostructural order–disorder phase transitions and anisotropic thermal expansions in polymorphic crystals of a biologically active molecule with distinct solubility and dissolution rate

Aditya Verma, Sourabh, Anil Kumar and Parthapratim Munshi *

Order–disorder phase transitions are common in inorganic and hybrid materials but are rare in single-component purely organic molecular crystals and are even scarcer in polymorphic crystals of biologically active molecules. Herein, we report the discovery of two polymorphic forms of a quinolone-amide-based biologically active molecule that undergo isosymmetric reversible order–disorder phase transitions at low temperatures, adopting crystal structures with low-to-high Z' values and exhibiting anisotropic thermal expansions. These studies were supported by variable-temperature X-ray diffraction experiments on single-crystals and powders of the dimorphs and by differential scanning calorimetry experiments. While the triclinic form undergoes a dynamic order–disorder phase transition at 150 K with a thermal hysteresis of ~10 K, the monoclinic form undergoes a similar transition at 170 K without thermal hysteresis. The molecules also experience a unique pedal-like motion. A detailed analysis of the molecular packing and energy frameworks establishes their distinctive identities, thereby describing these transitions as quasi-isostructural. The underlying mechanisms of the phase transition, molecular motion, and unusual thermal expansions are understood by examining nine sets of single-crystal X-ray diffraction data collected from 298 to 100 K for both polymorphs. Interestingly, the dimorphs display distinct equilibrium solubilities and intrinsic dissolution rates. This study offers valuable insights for establishing structure–property relationships in biologically active molecules and designing advanced materials with tunable biological and thermal properties.

Received 9th February 2025,
Accepted 12th February 2026

DOI: 10.1039/d5ma00114e

rsc.li/materials-advances

Introduction

Crystalline materials have been of practical importance in many scientific and technological fields. The defining nature and properties of such materials lie in their crystallographic structure. Not surprisingly, many examples of such materials exist that undergo a change in crystal structure when external stimuli such as light, pressure, or temperature are applied. Order–disorder phase transitions are one such example in which a material undergoes a phase change solely based on the extent of structural order it regains on applying a stimulus from a disordered state. Various systems, including metal–organic frameworks (MOFs),[1–4] hybrid perovskites,[5–7] metal nanoclusters,[8,9] and metal complexes,[10–12] have been reported to exhibit such behavior. Several mechanisms have been proposed to understand the nature of such transitions, the most common being the release of strain through molecular reorientation or the restriction of molecular movement. This phenomenon can lead to drastic changes in the mechanical, thermal, optical, and electronic properties of these materials. For instance, Jain *et al.* observed that the ordering of hydrogen atoms within a zinc-based MOF led to an order–disorder phase transition at ~156 K, with evidence of subsequent electric ordering from a paraelectric to an antiferroelectric phase.[1,2] Such transitions have also been understood as the mechanisms for establishing polymorphs,[12] *i.e.*, the ability of a compound to exist in multiple solid forms in pharmaceutical molecules, as reported by Petit and co-workers in the active pharmaceutical ingredient Ciclopirox.[13] Studies on the antihistamine desloratadine carried out by Florence *et al.* revealed a two-step, reversible, single-crystal-to-single-crystal (SCSC) phase transition between three of its polymorphs.[14] Similar transitions have also been observed in amino acid derivatives, such as in boc-L-methionyl glycine methyl ester from

---

Multifunctional Molecular Materials Laboratory, Department of Chemistry, School of Natural Sciences, Shiv Nadar Institution of Eminence Deemed to be University, NH-91, Tehsil Dadri, Gautam Buddha Nagar, Uttar Pradesh-201314, India. E-mail: parthapratim.munshi@snu.edu.in; Tel: +91-120-7170130

a high-to-low-Z' (number of crystallographically independent molecules in an asymmetric unit) crystal structure at 160 K,[15] in hydrophobic amino acids with linear side chains,[16] and in (quasi)racemic linear amino acids.[17]

Furthermore, in most crystalline materials, elongation or contraction of the crystallographic axes with heating or cooling results in a positive thermal expansion (PTE). However, there are special cases where some materials expand upon cooling and shrink upon heating, a phenomenon known as negative thermal expansion (NTE).[16,17] This intuitive phenomenon, induced by order–disorder phase transitions, has been commonly reported in perovskites,[18,19] metal complexes,[20–23] and MOFs.[24,25] In the case of molecular crystals, this phenomenon has been observed along one or two axes, which is compensated for by PTE along the other axes, leading to a small volumetric expansion.[26–30] NTE accompanied by a dynamic order–disorder phase transition in single-component organic molecular systems is seldom observed.[31,32] For instance, Takahashi *et al.* reported biaxial NTE and uniaxial PTE as the primary driving force behind a low-temperature order–disorder phase transition in 2,4-dinitro anisole.[32] Recently, some of us have studied a similar case of a reversible order–disorder phase transition accompanied by diverse anisotropic thermal expansions in an imidazole-based single-component molecular crystal, where the driving force of the transition was the rotational motion of the terminal –CF_3 group.[33] The study also demonstrated that the unusual thermal expansions resulted from the scissor-jack-like motion of the molecule within the lattice with the temperature variation. Carrying out variable-temperature X-ray diffraction experiments is well-suited to gain insight into disordered systems, as it can easily distinguish between static and dynamic disorder.

Investigating structure–activity relationships in medicinal chemistry is a common approach to identifying correlations between specific substitutions in drug molecules and their activity against a particular biological target. Along this line, the impact of different fluorine substitution patterns on the quinolone amide moiety has recently been explored against African sleeping sickness.[34,35] The study demonstrated that specific substitutions greatly enhanced the antitrypanosomal potency, while certain others led to a decrease or remained neutral. Therefore, examining structural properties of biologically active molecules, *i.e.*, the organic molecules that display biological effects in living organisms and play a crucial role in biological processes, is imperative. Moreover, many of these molecules can undergo polymorphic modifications and may display better or no activity against the target. Hence, studying such phenomena in crystalline materials is essential in establishing new crystal polymorphic forms with distinct properties and structure–property–activity relationships.[36]

In our continued effort to understand such phenomena in molecular crystals, we report the case of dimorphism in *N*-benzyl-1-butyl-6,8-difluoro-7-morpholino-4-oxo-1,2,3,4-tetrahydro quinoline-3-carboxamide (**1**, Scheme 1), a biologically active molecule.[34] While one of the polymorphs crystallizes in space group $P\bar{1}$ (**Form I**), the other crystallizes in space group $P2_1/c$ (**Form II**), both of which exhibit a dynamic and reversible order–disorder phase transition. While this occurs at ~150–160 K with a thermal hysteresis loop of ~10 K for **Form I**, a similar phenomenon occurs exactly at 170 K for **Form II** with no thermal hysteresis. Moreover, there is a doubling in the number of crystallographically independent molecules in the asymmetric unit, Z' from 1 to 2 after the phase transition for both the forms, with a noticeable variation in the unit-cell parameters, as established from nine sets of variable-temperature single-crystal X-ray diffraction (VT-SCXRD) data from 298 to 100 K. Further, low-temperature differential scanning calorimetry (DSC) and variable-temperature powder X-ray diffraction (PXRD) experiments have been carried out to complement the phase transition and its nature. A detailed analysis of the crystal structures, the molecular packing, and energy framework analyses for the HT (298 K) and LT (100 K) phases for each polymorphic form reveals that, though their structural arrangements are similar, upon closer examination, subtle differences between them establish the unique identity for each phase. Hence, these phase transitions are described as quasi-isostructural. While the isostructural phase transitions have been studied in organometallic systems,[37,38] the case of isostructural polymorphs has been established in organic molecular systems that exhibit equi-energetic crystal structures and molecular packing.[39,40] However, this study demonstrates polymorphism in a biologically active molecule and the unique quasi-isostructural characteristics of the variable-temperature phases in each polymorph, which interconvert *via* a dynamic order–disorder phase transition, accompanied by anisotropic thermal expansions. Further, we capture the structural dynamics and discover that the molecules undergo a unique pedal-like motion across the temperature range. Furthermore, we establish that both polymorphic forms remain thermally stable at elevated temperatures, with **Form II** being more thermally stable than **Form I**, as determined by thermogravimetric analysis (TGA), DSC, and hot-stage microscopy (HSM). The energetic stabilities of the polymorphs have also been compared. Additionally, we measure the equilibrium solubility and intrinsic dissolution rate (IDR) for the bulk (compound before crystallization) and the polymorphic forms to get insights into their bioavailability.

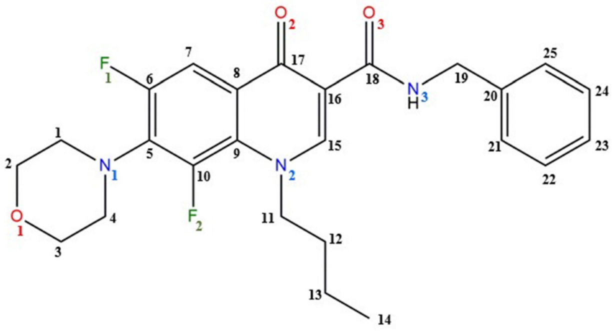

Scheme 1 Structure and characteristics of **1**.

Experimental section

Single-crystal X-ray diffraction

X-ray diffraction data sets on single-crystals of **Form I** and **Form II** were collected using a Bruker D8 VENTURE X-ray diffractometer equipped with a microfocus source (MoK_α), a PHOTON II CPAD detector, and a cryo-stream cryogenic system. The data were integrated and scaled using the APEX4 suite incorporated in the Bruker APEX4[41] software. A suitable colorless block-shaped crystal was selected for the X-ray diffraction experiments at various temperatures. The structures were solved by direct methods and refined by full-matrix least-squares on F^2 using SHELX-2014.2[42] implemented in Olex-2.[43] All non-hydrogen atoms were refined anisotropically, while the hydrogen atoms were positioned and refined isotropically.

Powder X-ray diffraction

The X-ray diffraction patterns of the powder sample of **1** were recorded using an Anton Parr XRDynamic 500 diffractometer equipped with a Primux 3000 Cu anode with CuKα radiation and a cryogenic system and Pixos 1000 detector. The sample was loaded into a quartz capillary, and the data were initially recorded at 300 K. The sample was then cooled at 2° min^{-1} and kept on an isotherm for 15 minutes. Subsequently, the data were recorded at 250, 200, 175, 160, 150, 140, 130, 120, 110, and at 300 K once again. At each temperature, the data were recorded in the 2θ range of 2° to 30° with a step size of 0.01°.

The experimental PXRD patterns on the dried samples of **1** and **Forms I** and **II** after the equilibrium solubility experiment were obtained on a Rigaku SmartLab multipurpose X-ray diffractometer equipped with monochromatic CuKα radiation with an acceleration voltage of 40 kV and a current of 30 mA. The diffraction patterns were recorded over 5–40° in 2θ with a scan rate of 5° min^{-1} and a step size of 0.01°.

Thermal characterization

TGA was performed on the powder sample of **1** and on the crushed single crystals of **Form I** and **Form II** at a 5 K min^{-1} scan rate using a Mettler Toledo TGA2 SF/1100 instrument. DSC measurements were carried out on each form at a scan rate of 2 K min^{-1} on a Mettler Toledo DSC3 instrument under a nitrogen atmosphere at a flow rate of 40 mL min^{-1}. Further, the low-temperature DSC measurements were carried out on the crushed single crystals of **Forms I** and **II** on a Mettler Toledo DSC3+ instrument from room temperature to 100 K at a scan rate of 2 K min^{-1} under a nitrogen gas atmosphere.

HSM studies on the single crystals of **Forms I** and **II** were carried out at a 5 K min^{-1} scan rate using a Nikon CFI60 infinity polarizing microscope equipped with a heating stage LTS420. The Linksys software was utilized to capture images and monitor crystal morphology.

Equilibrium solubility and intrinsic dissolution rate (IDR) experiments

The solubility and IDR of **1**, **Form I**, and **Form II** were measured in a 40% ethanol–water medium at 37 °C. First, the absorbance of a known concentration of each sample was measured at the $\lambda_{\max}$ of 289 nm using a Thermo Scientific Evolution 201 UV-vis spectrophotometer. The absorbance values were plotted against the known concentrations to prepare the calibration curve. An excess amount of the sample (30 mg) was placed in a glass vial containing 2 mL of the 40% ethanol–water media, and the mixture was stirred at 37 ± 5 °C for 24 hours at 800 rpm using a magnetic stirrer. Later, the suspension was centrifuged at 800 rpm for 1 minute and filtered to remove any excess solid material. Subsequently, the solution was diluted to achieve the desired absorbance. The experiment was repeated three times, and the absorbance values were finally fitted to a linear equation derived from the calibration curve. Thus, the amount of solubilized samples was quantified.

For the IDR study, the samples were ground to a homogeneous powder and tested on a U.S.P.-certified DS8000 dissolution rate apparatus. 100 mg each of **1**, **Form I**, and **Form II** were uniformly crushed using a mortar and pestle and were compressed at a pressure of 80 kg cm^{-2} for about 1 minute to form a pellet with a diameter of 1.2 cm. This pellet was dipped into a 500 mL solution of 40% ethanol–water with a paddle rotating at 120 rpm at 37 ± 5 °C. Then, 1.5 mL of the solution was withdrawn at fixed time intervals of 2, 4, 6, 8, 10, 15, 30, 45, 60, 90, 120, 150, 180, 240, 300, 390, 480, 600, and 750 minutes and was replaced with an equal volume of fresh media. Each sample was filtered with a 0.2 μm syringe filter, centrifuged at 800 rpm for 1 minute, and analyzed using a UV-vis spectrophotometer. The experiment was performed three times, and finally, the amount of drug dissolved in each time interval was calculated using the calibration curve.

Results and discussion

Synthesis and characterization

Compound **1** was synthesized following a previously reported method,[34,35] as detailed in the SI (Scheme S1). The formation of the final product was confirmed by characterizations of ^{1}H and ^{13}C nuclear magnetic resonance (NMR) (Fig. S1a and S1b) and high-resolution electrospray ionization mass spectrometry (HR-ESIMS) (Fig. S1c).

Crystallization

Single crystals of **1** were grown in HPLC-grade solvents using the vapor diffusion and slow evaporation methods (Tables S1 and S2). High-quality, colorless, block-shaped crystals of **Form I** grew *via* the vapor diffusion method in a 1 : 1 ratio of ethyl acetate and hexane at 4 °C (Fig. S2a). Also, block-shaped crystals of **Form II** were obtained by slow evaporation method in methanol at 4 °C (Fig. S2b). While crystals of **Form II** were obtained by large-scale crystallization of the bulk compound (∼70 mg at a time) in various solvents, the kinetically favored **Form I** crystals were obtained only through smaller crystallization batches of ∼5 mg at a time.

Crystal structure analysis

Excellent quality single crystals of **Form I** and **Form II** were selected for the X-ray diffraction experiments. Crystallographic data and the associated refinement parameters are listed in Tables S3 and S4. Crystal structure determination from the data at 298 K confirms that while **Form I** crystallizes in the triclinic

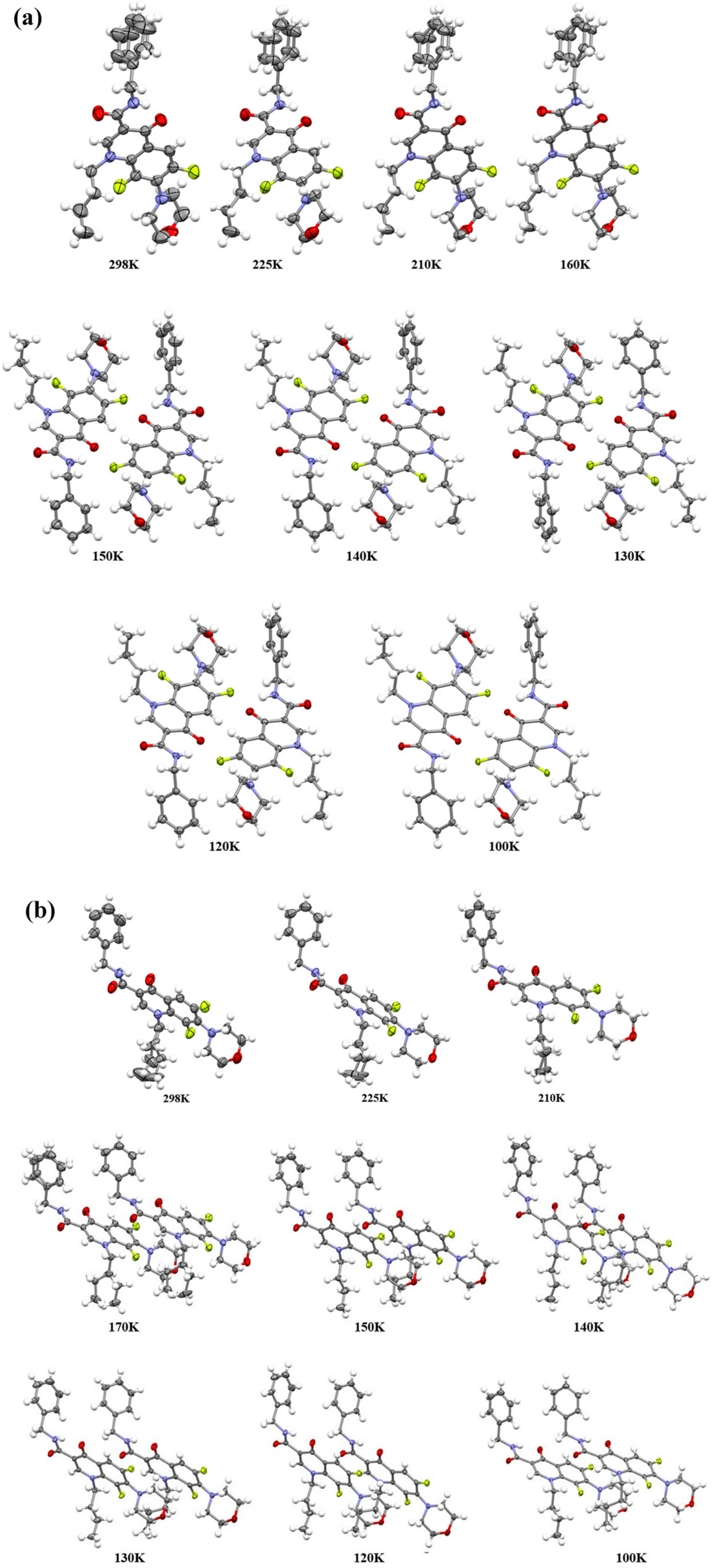

Fig. 1 Thermal ellipsoid plots (drawn at 50% probability) of the asymmetric unit of (a) **Form I** for its HT (298–160 K) and LT (150–100 K) phases and of (b) **Form II** for its HT (298–210 K), intermediate (170 K) and LT (150–100 K) phases. H atoms are represented as the fixed spheres.

crystal system with space group $P\bar{1}$ and $Z' = 1$, **Form II** crystallizes in the monoclinic crystal system with space group $P2_1/c$, and also with $Z' = 1$. The crystal structures (Fig. 1) of both polymorphs reveal positional disorder, specifically the terminal benzene ring for **Form I** and the terminal butyl chain for **Form II**. Naturally, data were also collected at 100 K, which resulted in a completely ordered structure of **Form I** with space group $P\bar{1}$ and $Z' = 2$ (Table S3), but with a set of distinct unit cell parameters, and similarly so for **Form II** with space group $P2_1/c$ and $Z' = 2$ (Table S4), indicating that **Forms I** and **II** undergo isosymmetric, SCSC, disordered-to-ordered phase transitions upon cooling. It was noticed that the unit cell edge length *a* of both forms almost doubled (increased approx. 95% for **Form I** and 113% for **Form II**) after the transition. However, upon transforming *a* to *a*/2 and other cell parameters accordingly, the structures at 100 K could not be refined with the cell parameters similar to those at 298 K; the *R*-factors were unusually high ($>11\%$), the thermal ellipsoids of most of the atoms were unusually low or high, and the structures were partially disordered. Further, either weak diffuse diffraction features or satellite reflections were not obvious from a thorough scrutiny of the diffraction data sets (see Annexure S1). The analysis also suggests that the LT phases of **Form I** and **Form II** do not undergo positional modulation, unlike in a few other cases reported in the literature.[44,45] Nevertheless, to check if the LT phases of both forms adopt superstructures, their diffraction peaks were indexed with the modulation wave-vector, *q*. The corresponding *q*-vectors, along with their estimated standard deviations (σ), and the structural refinement statistics are listed in Tables S5 and S6. Although in both forms the *q*-vector values are greater than their 3σ values, in **Form I**, the refinement parameters and the maximum/minimum electron density peaks are significantly higher than those obtained without the *q*-vector refinements. Moreover, in the case of **Form II**, the structures could not be refined with reasonable atomic displacement parameters and *R*-factors using the diffraction data collected at LT, except at 100 K. Nonetheless, the above analyses indicate that the LT structures are ordered superstructures of the HT disordered structures.

Variable-temperature single-crystal X-ray diffraction study

Further, to probe the phase transition behavior, the unit-cell parameters of **Form I** and **Form II** crystals were determined at 298 K, 280–160 K at 20 K intervals, and 150–100 K at 10 K intervals. The experiment reveals that, upon cooling, to 150 K, **Form I** experiences a significant change of 100.1% along the *a*-axis and marginal changes of 0.67% and 0.11% along the *b* and *c*-axes, respectively, while the overall volume increases by 100.21% (Table S7). A similar trend in the variation of the unit-cell parameters was noticed while heating from 100 K to 298 K. However, the changes were seen after 160 K (Table S8). Such variation in cell parameters (Fig. S3) suggests that **Form I** undergoes a reversible phase transition between 150 and 160 K, with a thermal hysteresis of ∼10 K. The inspection of the variation of the unit cell edge lengths (Δl) and volume (ΔV) with respect to the variation of temperature (ΔT) before (298–160 K) and after (150–100 K) the phase transition reveals that **Form I** experiences anisotropic thermal expansions (Table S9). Upon cooling, the *a*-axis undergoes a usual moderate contraction (PTE) before and after the phase transition, and the *b*-axis experiences a significant contraction before the phase transition but contracts marginally after the transition. Interestingly, the *c*-axis, with oscillation, displays an unusual expansion before the phase transition, signaling an NTE behavior, and a PTE trend, also with oscillation, after the phase transition, leading to a slight expansion of *V* before and after the transition.

For **Form II**, upon cooling, to the phase transition temperature of 170 K, the *a*-axis undergoes a significant expansion by ∼103%, the *b*-axis contracts by 4.13%, and the *c*-axis expands by 1.40%. Further, the angle β contracts by 1.69% while the volume increases by 97% (Table S10). A similar trend in the variation of unit cell parameters was observed during heating from 100 to 298 K (Table S11), suggesting that this is also reversible phase transition. However, unlike **Form I**, the phase transition occurred again at 170 K, with no thermal hysteresis (Fig. S4). Further, the variation of Δl and ΔV with ΔT before (<170 K) and after (>170 K) the phase transition reveals that upon cooling from 298 to 100 K, the *a* and *c*-axes undergo a moderate to significant contraction before and after the phase transition (Table S12). Interestingly, the *b*-axis undergoes a significant unusual expansion before the phase transition, signaling an NTE effect. However, it experiences a moderate expansion after the phase transition. It is also noteworthy that the unique angle β expands with decreasing temperature, leading to a slight expansion of *V* before and after the transition.

Order–disorder phase transition

To gain insights into the structural changes due to the temperature variation, SCXRD data sets were collected at 298, 225, 210, 160, 150, 140, 130, 120, and 100 K for **Form I** and at 298, 225, 210, 170, 150, 140, 130, 120, and 100 K for **Form II**. The subsequent structure determinations reveal that the space group ($P\bar{1}$) of **Form I** remains unchanged for the entire temperature range. However, Z', with a value of 1 up to 160 K, changes to 2 at 150 K and remains constant until 100 K, along with almost doubling the unit-cell edge length *a* and the volume *V* (Table S3). A similar analysis on **Form II** also reveals that the space group ($P2_1/c$) remains unchanged for the entire temperature range. However, the crystal structures with Z' of 1 between 298 and 210 K transform to crystal structures with Z' of 2 at 170 K and remain constant thereafter till 100 K, along with similar significant changes in the unit-cell edge length *a* and the volume *V* (Table S4). In a few earlier reports, although such structural transformations have been categorized as modulated structures,[46,47] in these two cases of polymorphs, our complementary DSC and PXRD (discussed in later sections) studies affirm that these are cases of phase transitions. The analysis of crystal structures demonstrates that both the polymorphs undergo an isosymmetric, SCSC, and disorder-to-order structural transformation at LT (Fig. 1). The modelled disorder in the crystal structures, as represented by the free rotation of the terminal benzene ring about the C19-C20 bond for **Form I**, persists in the temperature range from 298–160 K (Fig. 1a). Finally, the crystal structure becomes ordered at the phase transition temperature of 150 K. However, the atomic disorder reappears in the terminal benzene ring upon reheating. Hence, this is a case of order–disorder phase transition induced by the free rotation of the terminal benzene ring. For **Form II**, the modelled disorder in the variable-temperature crystal structures (Fig. 1b) reveals free rotation of the terminal butyl chain about the C11–C12 bond, which persists over the temperature range 298–210 K. However, at the phase transition temperature of 170 K, the free rotation in the butyl chain reappears in both molecules. Additionally, the terminal benzene ring in one of the two independent molecules experiences a free rotation about the C19–C20 bond. Such disorders suggest that the structure at 170 K is intermediate between the HT and LT phases. Subsequently, the crystal structure becomes ultimately ordered at 150 K, suggesting **Form II** also undergoes an order–disorder phase transition. Moreover, in both forms, before the phase transition, the site occupancy varies with temperature (63 : 37 to 47 : 53 for **Form I** and 80 : 20 to 75 : 25 for **Form II**), suggesting that the disorders are dynamic in nature.

Molecular conformations and structural dynamics

To gain insight into the conformational changes in the molecules of the crystal structures of **Form I** and **Form II** due to the phase transition, a molecular conformation analysis was conducted by overlaying the molecules of the crystal structures at variable temperatures and quantifying the conformational differences by the root-mean-square-deviation (RMSD), as incorporated in the program Mercury.[48] The RMSD analysis was carried out by superimposing the molecule of the major conformer of the HT phase in the asymmetric unit with each of the crystallographically independent molecules of the LT phase. For **Form I**, the high RMSD values confirm the stark differences in the molecular conformation between the two phases (Fig. S5a). In contrast, molecule A in the asymmetric unit of the LT phase is conformationally unique and independent of that in the HT phase; molecule B has a conformation similar to that in the HT phase. A distinct conformational difference is also noticed between the two independent molecules in the asymmetric unit of the LT phase (Fig. S5a). A similar set of analyses for the variable temperature crystal structures of **Form II** also reveals distinct conformational changes; unlike **Form I**, the overlay of the molecule at HT with each of the molecules at LT shows that they have different conformations, as also reflected from the large values of the RMSD (Fig. S5b). However, the two independent molecules in the asymmetric unit of the LT phase adopt a similar conformation (Fig. S5b).

Further, to capture the structural dynamics of **Form I** and **Form II** and their HT and LT phases with temperature variation, structural overlay between the molecules of the crystal structures was performed with respect to the C16–C18–N3–C19 bonds using Mercury. The analysis reveals that in the HT phase ($Z' = 1$) of **Form I**, the molecule undergoes a pedal-like motion between the temperatures 298 K and 210 K; the molecule at 225 K adopts a conformation that is related by approximately 2-fold rotation about its longest axis with respect to the molecule at 298 K and reverts to the original conformation at 210 K (Fig. 2a). Finally, the molecule at 160 K acquires a similar conformation to that at 298 K. The pedal-like motion has been further quantified by comparing the dihedral angle ∠C18–N3–C19–C20 in the asymmetric unit of the structures between 298–160 K (Table S13). However, the molecular motion observed in this case is unlike the typical disorder-induced pedal motion observed in azobenzene structures.[49,50] Interestingly, while comparing the molecular orientations in the LT phase ($Z' = 2$) of **Form I**, we observed that the terminal benzene ring in both the molecules within the unit cell of the crystal structure at 130 K adopts a different conformation, which reverts to its original conformation at 120 K and beyond, as was the case with the conformations at 140 and 150 K (Fig. 2b). A geometrical analysis of the asymmetric unit at 130 K with that of 120 and 140 K reveals an out-of-plane movement ($\sim 40^\circ$) of the benzene ring, as measured from the dihedral angles, ∠N3-C19-C20-C25 (Table S11). Further, upon comparing the structure at 160 K with those at 130 and 150 K, it turns out that one of the two molecules of the structures at 150 and 130 K adopts the major and minor conformers of the structure at 160 K, respectively (Fig. 2c). The structural overlay analysis of **Form II** reveals that not only the molecule ($Z' = 1$) in the HT phase (Fig. 2d) but also the molecules ($Z' = 2$) in the LT (Fig. 2f) phase undergo the pedal-like motion as described for the HT phase of **Form I**. The conformational change from the HT to LT phase through the intermediate phase (170 K) is also highlighted in Fig. 2e.

Further, the overlay (Fig. S6) of the major conformer of the molecule of **Form I** at 298 K and that of **Form II** resulted in an RMSD of 0.284 Å ($<$0.375 Å), suggesting that these are not conformational polymorphs.[51]

Molecular packing similarity analysis

The packing of the molecules of **Form I** in the crystal structure of the HT (298 K) phase (Fig. S7a) is primarily governed by intermolecular C–H···O, C–H···F, and N–H···F hydrogen bonds, leading to the formation of a ripple-like layered structure (Fig. S8a). A similar packing is also seen for the LT (100 K) phase (Fig. S7b). The molecular layers are stacked *via* C–H···π interactions (Fig. S8b). When viewed down the *b*-axis, subtle differences are noticed in the molecular arrangements in the HT and LT phases (Fig. 3a); the relative orientation of the central portion of the molecule (encircled in red) shows some distinct changes. These observations suggest that although the molecular packing in the crystal lattices of the phases before and after the phase transition is similar, subtle differences in the molecular arrangement highlight their uniqueness. Therefore, they are described as quasi-isostructural phases that interconvert *via* a quasi-isostructural phase transition, a unique case in this class of phase transitions. Similarly, for **Form II**, the packing of the molecules in the crystal structure of the HT and LT phases is primarily governed by intermolecular C–H···O and C–H···F hydrogen bonds (Fig. S9). A closer look at the molecular packing arrangement in both phases, when viewed down the *c*-axis, also points to the subtle quasi-isostructural features; a good example of this is the relative arrangement of the terminal butyl chains and the morpholine moiety (encircled in red) in the HT and LT

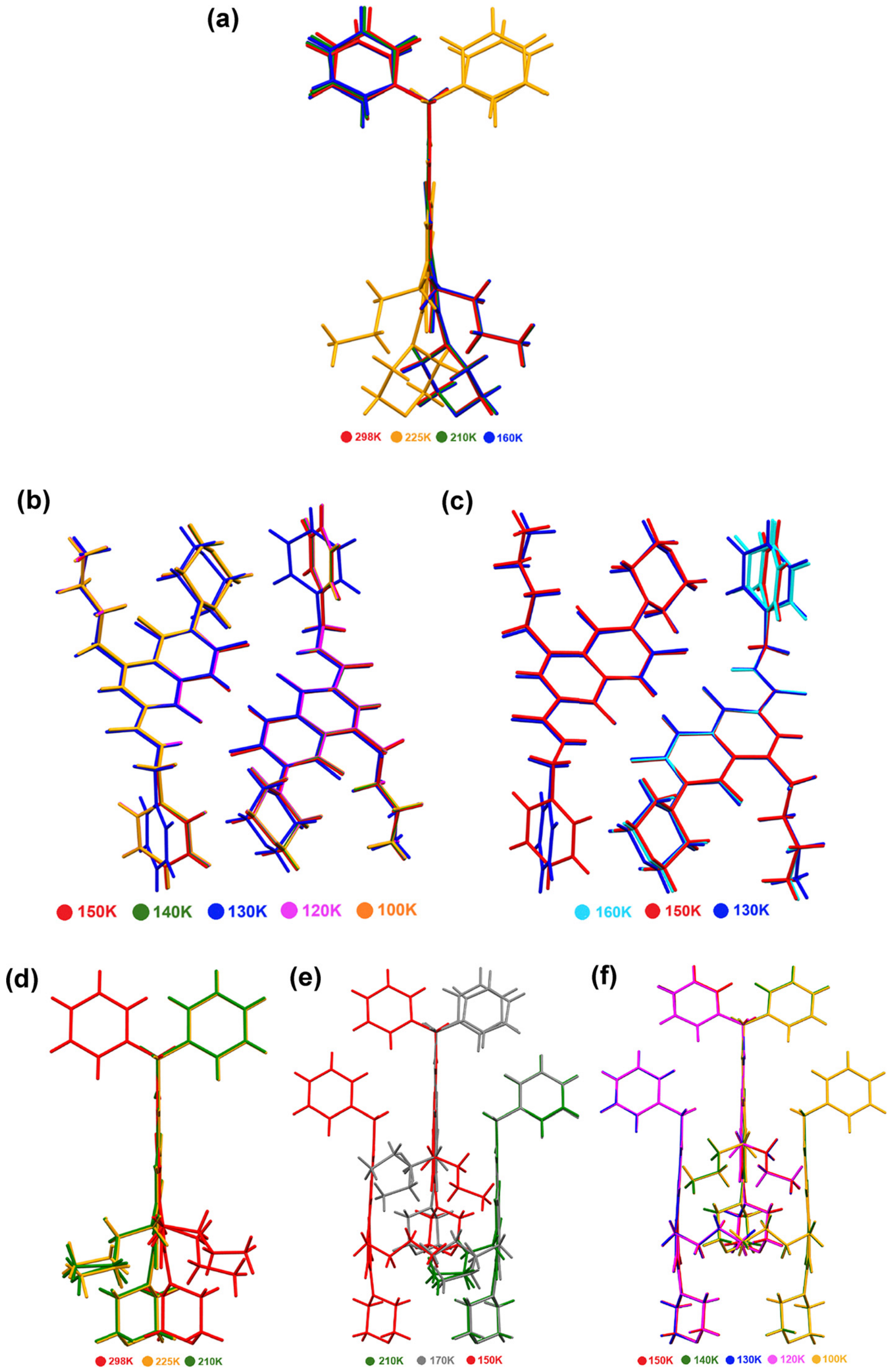

Fig. 2 Structural overlay with respect to the C16–C18–N3–C19 bonds of the molecules at the (a) HT and (b & c) LT phases of **Form I** and (d) HT, (e) intermediate, and (f) LT phases of **Form II**.

phases, even though the overall packing arrangement is quite similar (Fig. 3b).

To further ascertain the nature of the quasi-isostructural features and understand the differences between the HT and LT phases of both the polymorphic forms, a crystal packing similarity was performed using Mercury (Fig. S10). The results reinforce the unique structural features of each phase, although the similarity is greater for **Form I** (RMS: 0.305) than that for **Form II** (RMS: 0.499). Further, comparing the simulated PXRD patterns of the HT and LT phases of **Form I** (Fig. S11) and **Form II** (Fig. S12) highlights the differences and similarities between the two phases. For **Form I**, the subtle differences in the peak positions, especially at the higher 2θ positions, support the quasi-isostructural characteristics of the phase transition. A similar comparison for **Form II** results in a higher degree of dissimilarity, which correlates well with the

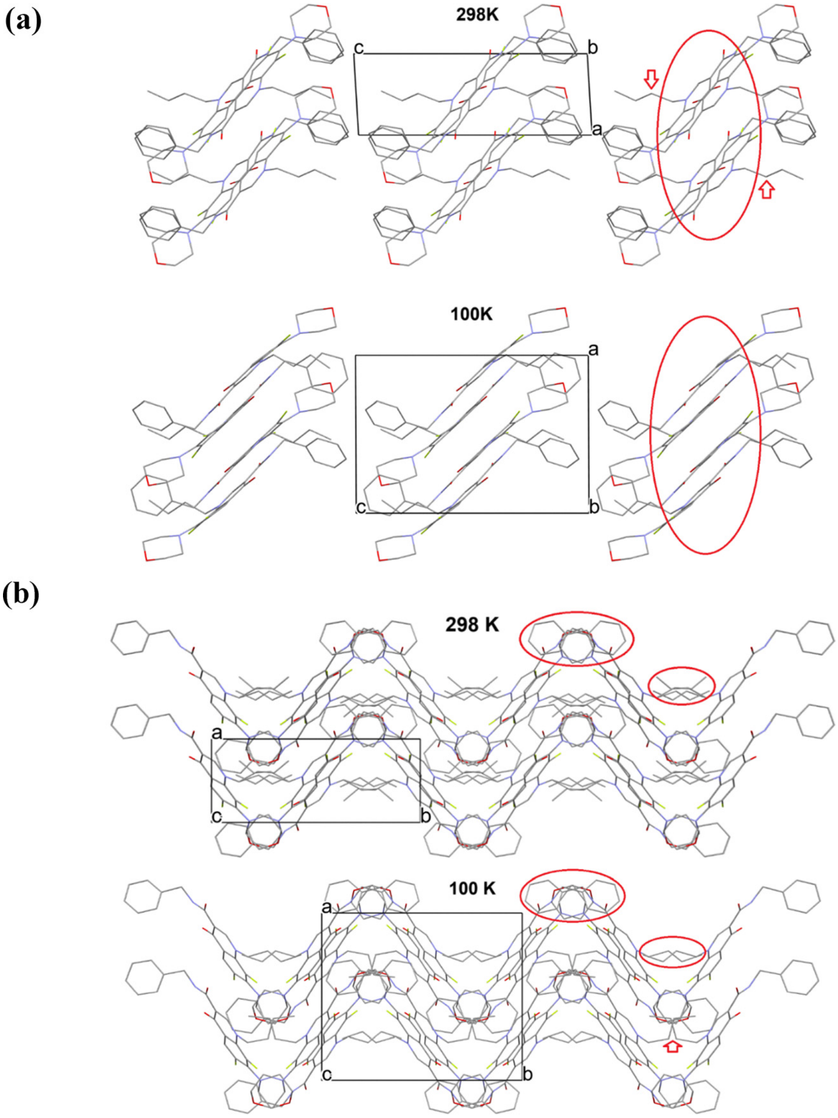

Fig. 3 Molecular packing arrangement of the HT and LT phases of (a) **Form I** and (b) **Form II**, highlighting the quasi-isostructural features in each. Hydrogen atoms are not shown for clarity.

structural packing similarity analysis, suggesting that this is also a case of a quasi-isostructural phase transition. The distinct molecular packing between the structure of **Form I** at 298 K and that of **Form II** suggests that these are packing polymorphs.[52]

Intermolecular interaction energies and lattice energies

To understand the nature of the interactions and compare those between the structures at 298 K (HT phase) and 100 K (LT phase) of **Form I** and **Form II**, Hirshfeld surfaces and the associated fingerprint plots for both phases were generated using CrystalExplorer 21.5.[53] (Fig. S13 and S14). All the calculations discussed in this section were performed based on the crystal geometries, and for the HT phases, only the major conformer was considered. A careful examination of the Hirshfeld surfaces and the inspection of the contributions of the major interactions, as reflected in the fingerprint plots, reveal qualitative and quantitative differences between the two phases in each form. Further, to construct energy frameworks[54] for the HT and LT phases of each polymorph, pairwise intermolecular interaction energies (IE) were calculated using Gaussian09[55] at the B3LYP/6-31G(d,p) level of theory,[56] after normalizing the C-H and N-H bond distances to 1.083 and 1.009 Å, respectively (Table S14). The subtle differences in the arrangement of the various energy elements (rods, crossbars, and strings) highlight the quasi-isostructural features of the HT and LT phases for each polymorph (Fig. S15 and S16). Subsequently, we estimated lattice energy, following a procedure reported by Spackman *et al.*[57] For **Form I**, the calculated lattice energies of the HT and LT phases are −207.1 and −227.3 kJ mol^{-1}, respectively, while those of **Form II** are −213.5 and −238.4 kJ mol^{-1}, respectively.

Further, based on the same crystal geometries used in the IE calculation, molecular packing energies were calculated using the UNI force field *via* Mercury.[47] The energies follow a similar

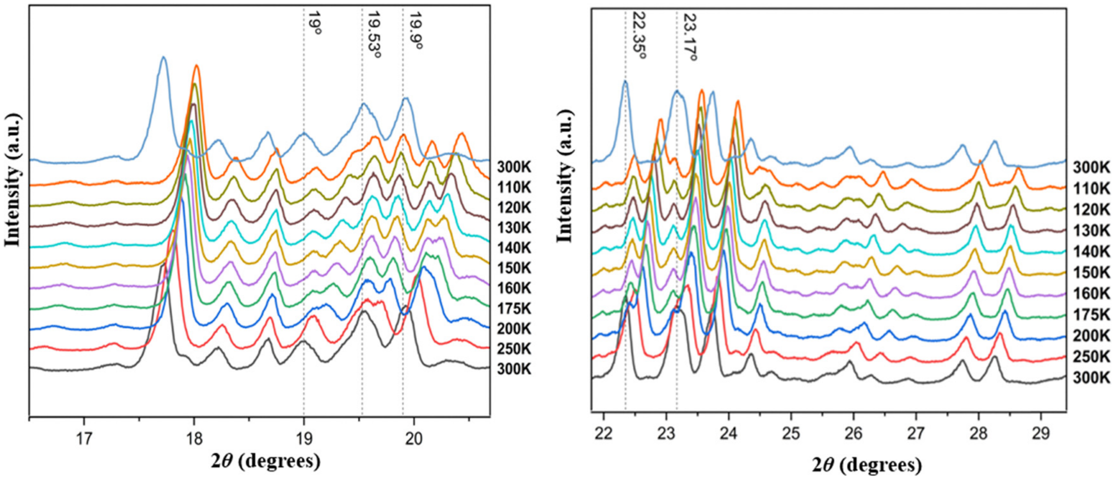

Fig. 4 PXRD pattern of **Form I** recorded from 300 to 110 K during the cooling and at 300 K during the heating cycles. Reference dotted lines depict the changes in the pattern.

trend to those listed above; for **Form I**, the HT phase has a higher packing energy (-203.0 kJ mol^{-1}) than the LT phase (-213.9 kJ mol^{-1}), and those of **Form II** are -221.3 kJ mol^{-1} and -222.8 kJ mol^{-1}, respectively.

Furthermore, the PIXELC[58] method implemented in the CLP module was used to estimate the lattice energies using Gaussian09 at the B3LYP/6-31G(d,p) level of theory using the same crystal geometries as used for the above calculations. For **Form I**, the estimated lattice energies of the HT and LT phases are -173.2 and -189.8 kJ mol^{-1}, respectively, and those of **Form II** are -180.3 and -187.7 kJ mol^{-1}, respectively.

The estimated energies obtained using different approaches correlate well and indicate that the ordered LT phase is more stable than the disordered HT phase for both polymorphs. This is expected due to the lower temperature, which leads to an energetically stable structure. Moreover, these results suggest that the polymorph **Form II** is energetically more stable than **Form I**.

Variable-temperature powder X-ray diffraction study

Further, the phase transition behavior was studied based on the PXRD experiments on **Form I** by collecting data while cooling from 300–110 K (Fig. S17a). A noticeable change in the peak positions and the overall patterns in the stacked VT-PXRD patterns at 2θ of ∼19°, ∼19.5°, ∼20°, ∼22°, and ∼23° indicates the phase transition behavior of **Form I** (Fig. 4). At around 175 K, the peaks shift slightly to the right at all the indicated 2θ values and split completely from a singlet to a doublet at the phase transition temperature of 150 K, as ascertained from the VT-SCXRD experiments. These changes are highlighted by comparing the PXRD patterns at 300 K and 150 K (Fig. S17b). Further, the reversibility of the transition is confirmed by observing the PXRD pattern at 300 K after the complete cooling cycle; the peak positions and features are like those obtained at the start of the experiment at 300 K. The VT-PXRD experiment was not performed for **Form II**, as both the polymorphic forms follow a similar phase transition behavior.

Thermal analysis

The relative thermal stabilities of **Forms I** and **II** as compared to **1**, as seen from the respective TGA thermograms (Fig. S18a–c), reveals that **Form II** is thermally the most stable form, with a complete mass loss occurring at an elevated temperature of 372.83 °C (645.83 K), as compared to 359.5 °C (632.5 K) for **Form I** and at 356.5 °C (629.5 K) for **1**.

The DSC thermograms recorded for **1**, **Form I**, and **Form II** reinforce the higher melting point of **Form II** compared to **Form I** and the phase stability of each polymorphic form (Fig. S19a–c). During the first heating, the thermogram of **1** shows a broad melting peak at 128.4 °C (401.4 K), and the second heating cycle exhibits an endothermic peak at 131.1 °C (404.1 K). **Form I** melts at 130.2 °C (403.2 K), and the second heating cycle results in an endothermic peak at 130.3 °C (403.3 K), which is at par with the melting peak observed in the first cycle, indicating the phase stability of **Form I** (Fig. S20b). The higher melting point of **Form II** than **Form I** is immediately established due to the endothermic peak at a slightly elevated temperature of 131.3 °C (404.3 K) seen in the first heating cycle of the thermogram (Fig. S19c). The second heating and cooling cycles reveal similar thermal characteristics, indicating the phase stability of **Form II**. Interestingly, the endothermic peak in the second heating cycle corresponds exactly to the peak observed in the same cycle in the thermogram of **1**, suggesting that the bulk form transforms into **Form II** upon heating and cooling.

Further, low-temperature DSC experiments were conducted on crushed single crystals of both forms to gain insights into the temperature dependence of the phase transitions observed in **Form I** and **Form II**. The studies yield complementary results to those obtained from the VT-SCXRD experiments. The thermal characteristics, as shown in Fig. 5a, show that **Form I** is thermally stable and does not reveal any thermal behavior until 220 K, and then exhibits two endothermic peaks at 218.66 K and 149.4 K, and one sharp exothermic peak at 132.46 K. The phase transition temperature of

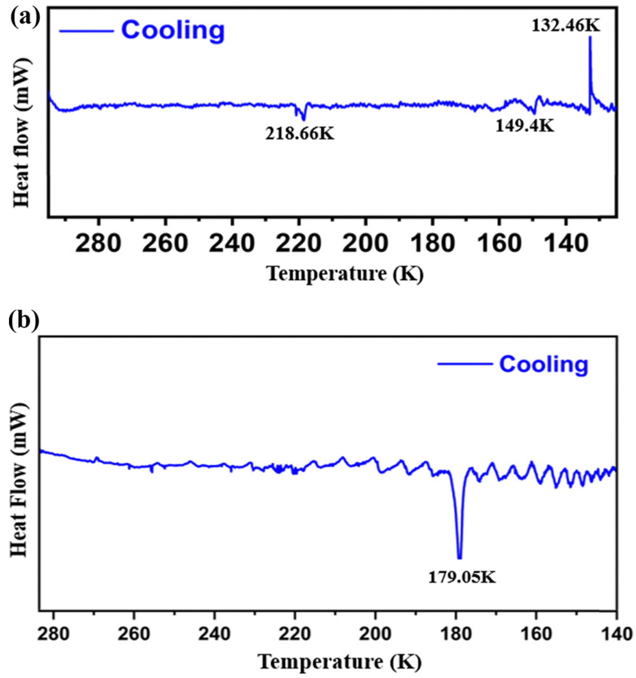

Fig. 5 Low-temperature DSC thermograms recorded in the temperature range of (a) 298–120 K for **Form I** and (b) 283–140 K for **Form II**.

150 K, as observed from the VT-SCXRD data, corresponds to the endothermic peak at 149.4 K. The exothermic peaks at ~219 and ~132 K correlate well with the conformational change in the crystal structure at 225 and 130 K, as seen from the corresponding crystal structures (Fig. 2a and b). A similar analysis of **Form II** (Fig. 5b) shows an endothermic peak at ~179 K, consistent with the results of the VT-SCXRD experiment, which confirmed the phase transition temperature to be ~170 K. The change in enthalpy, ΔH, corresponding to the endothermic peaks at ~149 K for **Form I** (Fig. 5a) and at ~179 K for **Form II** (Fig. 5b) is 57.7×10^{-3} and 259.21×10^{-3} J g^{-1}, respectively, asserting that **Form II** is thermodynamically more stable than **Form I**, which is in accordance with their energetic stabilities.

Further, the phase and crystal morphological stability of both polymorphic forms with respect to temperature were probed *via* HSM under identical conditions for each polymorph. For **Form I** (Fig. S20a), the crystals remained intact until ~133 °C (406 K), at which point some loss of epitaxial domains occurred before completely melting at ~148 °C (421 K). A similar analysis of the crystals of **Form II** (Fig. S20b) displays some epitaxial domain loss at ~139 °C (412 K) before completely melting at ~154 °C (427 K). These results are reasonably consistent with those from the corresponding DSC thermograms and reinforce the higher thermal stability of **Form II** compared to **Form I**.

Anisotropic thermal expansion

The extent of thermal expansion was estimated by calculating the linear coefficient of thermal expansion (CTE) for the HT and LT phases of **Form I** and **Form II** using the PASCal program.[59]

In **Form I**, while the HT phase experiences a slight NTE along the $X1(\alpha_{X1})$ direction, a moderate to colossal biaxial PTE along the $X2(\alpha_{X2})$ and $X3(\alpha_{X3})$ directions, respectively, and a low volumetric CTE of ~189(6) MK^{-1}, the LT phase exhibits moderate uniaxial NTE effect along $X3$ direction and low to colossal biaxial PTE effect along the $X2$ and $X1$ directions, respectively (Table S15). Similar CTE values were also observed in some other single-component organic molecules.[27,60] Interestingly, the LT phase also experiences a negative area expansion involving the two principal axes $X2$ and $X3$, with a CTE value of −39.2 MK^{-1}. This results in a very low volumetric CTE of ~107(19) MK^{-1}, lower than those reported earlier.[27–29] In the case of **Form II**, while the HT phase exhibits a large uniaxial NTE (−75.7(9.4) MK^{-1}) along the $X3$ direction that coincides with the crystallographic *b*-axis, a low to super colossal biaxial PTE is observed along the $X2$ and $X1$ directions, respectively. In the HT phase, a large negative area expansion (−65.2 MK^{-1}) is also observed involving the two principal axes $X2$ and $X3$. This results in a very low volumetric CTE of ~167(26) MK^{-1}. A low to moderate PTE for the LT phase along all three principal axes, $X1$, $X2$, and $X3$, resulted in a low volumetric CTE of ~117(12) MK^{-1} (Table S16). Further, the variation of the principal axes (X) with temperature for both polymorphs, as depicted in Fig. 6, highlights that the NTE effect in the HT phase of **Form II** is significant (>1% change in X with temperature),[60] whereas that in the HT and LT phases of **Form I** is negligible. The indicatrix plots qualitatively represent the thermal expansivity tensor and illustrate the behavior of the CTE along the X for the HT and LT phases of both polymorphs, as shown in Fig. S21. The uniaxial NTE effects for the LT phase of **Form I** and the HT phase of **Form II** are depicted by the blue surface, while the colossal PTE in the HT phase of **Form I**, represented by the large red surfaces, masks its moderate NTE effect.

Corroborating the above results, we infer that the possible mechanism that drives the phase transitions at LTs is due to the free rotation of the terminal benzene ring and the terminal butyl chain that allows for a rearrangement of individual molecules within the unit cell and its subsequent expansion when the optimum conformation is achieved upon this free rotation. The quasi-isostructural features observed during the phase transition also highlight this, due to the subtle differences in the molecular packing within the crystal lattice between the HT and LT phases.

Equilibrium solubility and intrinsic dissolution rate

The promising biological activity of **1**, the quinolone-amide-based compound,[35] and the gripping physical properties exhibited by its two polymorphic forms prompted us to measure equilibrium solubility and IDR on the bulk form (**1**), **Form I**, and **Form II** to gain insight into their bioavailability. The calibration plots for each form are depicted in Fig. S22. The results suggest that **Form II** is the most soluble in the 40% ethanol–water media, followed by **Form I** and **1** (Table 1). Despite **Form II** being energetically and thermodynamically more stable than **Form I** in its crystalline form, the latter is more stable

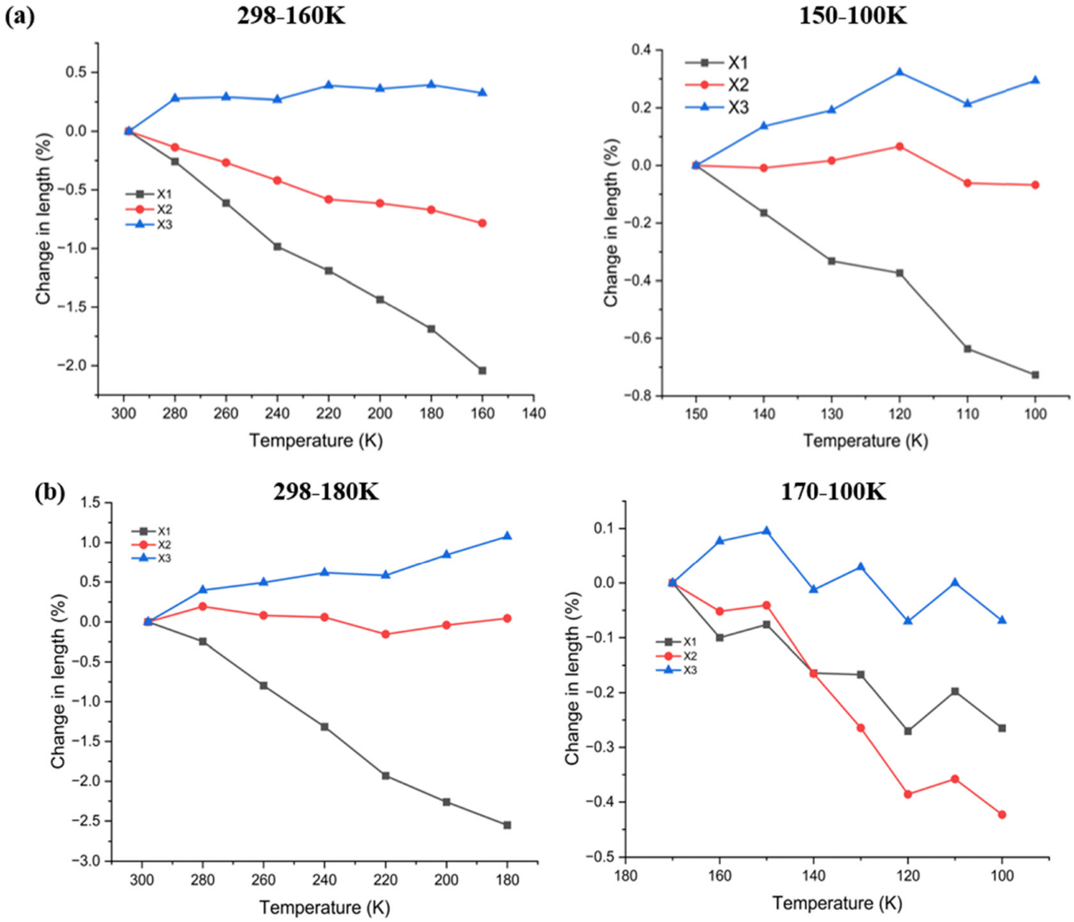

Fig. 6 Percentage change in the length of the principal axes (*X*) with the change in temperature for (a) **Form I** and (b) **Form II**. The temperature range specified for each plot is in bold.

Table 1 Equilibrium solubility and IDR of **1**, **Form I**, and **Form II**

Sample	Equilibrium solubility (mg mL^{-1})	IDR (mg cm^{-2} min^{-1})
1	0.397(±0.010)	0.0213
Form I	0.760(±0.027)	0.0596
Form II	1.225(±0.002)	0.0904

in solution than the former. Thus, the metastable **Form II** is the preferred form from both shelf-life and bioavailability viewpoints. The samples recovered after the IDR experiments were dried and analyzed by PXRD to determine their phases. The identical PXRD patterns before and after the IDR experiments confirm that both the polymorphic forms retain their phase even after mechanical grinding and solubilizing (Fig. S23a–c).

The IDR experiments also reveal that in the same media, the dissolution rate of **Form II** is the fastest, and that of the bulk form, **1**, is the slowest (Fig. 7). The results (Table 1) obtained from the IDR experiments correlate very well with those from the equilibrium solubility measurements, proving that **Form II** is indeed the metastable form in its solution phase. Notably, the polymorphic forms have superior equilibrium solubility and IDR than **1**.

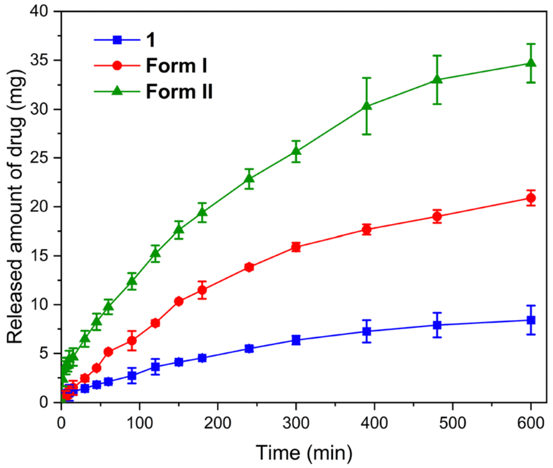

Fig. 7 IDR profile of **1**, **Form I**, and **Form II** in 40% ethanol–water media.

Conclusion

This study demonstrates that **1**, a quinolone amide-based biologically active compound, exists in two polymorphic forms, **Form I** and **Form II**, with **Form I** being the kinetically favored crystal form. The dimorphs undergo isosymmetric disorder-order phase transitions and adopt crystal structures from low-to-high Z' values at low temperatures. While **Form I** undergoes a reversible phase transition at $\sim$150 K with a thermal hysteresis of $\sim$10 K, **Form II** shows a reversible phase transition at 170 K without a thermal hysteresis, demonstrating the scope of tuning thermal hysteresis *via* polymorphic modifications. Structural disorders occur during the HT phase of **Form I** and **Form II** due to the free rotation of the terminal benzene ring and the butyl chains, respectively. A careful analysis of nine sets of VT-SCXRD data reveals that the molecules in their crystal lattice undergo a unique pedal-like motion, especially in **Form II**. Further, the molecular packing analysis of the HT and LT phases of both forms reveals similar structural features overall. However, subtle differences in the relative positions of various sections of the molecular arrangement within the lattice differentiate the two. These established the unique identity of each phase, apart from variations in the unit cell parameters, effectively denoting that these phases are quasi-isostructural to each other and that they interconvert *via* a quasi-isostructural phase transition. Additionally, **Form II** exhibits a significant uniaxial NTE and moderate PTE before and after the phase transition, respectively. Interestingly, both forms exhibit negative thermal-area expansions in their HT phases. Further, the thermal analysis and the estimated lattice energies confirm that **Form II** is thermally and energetically more stable than **Form I**. Furthermore, based on the IDR and equilibrium solubility studies, it is established that **Form II** is the metastable form. Therefore, **Form II** is the preferred polymorph from both shelf-life and bioavailability viewpoints. However, storing this potential bioactive molecule at low temperatures may hamper its efficacy, as it undergoes phase transitions and adopts an alternate conformation with temperature variation. The findings reported in this study are crucial for designing advanced materials, establishing structure–property relationships in biologically active molecules with multifunctional properties, understanding their behavior under adverse temperature conditions, and gaining insights into bioavailability improvement.

Author contributions

Conceptualization, P. M.; methodology, A. V., Sourabh, and A. K.; investigation, A. V., A. K., Sourabh, and P. M.; writing – original draft, A. V. and P. M.; writing – review & editing, A. V. and P. M.; funding acquisition, P. M.; resources, P. M.; supervision, P. M.

Conflicts of interest

There are no conflicts to declare.

Data availability

The data supporting this article have been included as part of the supplementary information (SI). Supplementary information: synthesis, NMR and HR-ESIMS spectra, crystallization details, optical images of crystals, crystal data, and refinement parameters, unit-cell parameters at variable temperature, molecular packings, Hirshfeld surfaces, fingerprint plots, interaction energies, energy frameworks, PXRD, TGA, DSC, *etc.* plots, HSM images, the values and plots relevant to thermal expansion studies, the calibration plots for the equilibrium solubility studies, and diffraction data analysis details as Annexure S1. See DOI: https://doi.org/10.1039/d5ma00114e.

CCDC 2386800–2386816 and 2386889 contain the supplementary crystallographic data for this paper.[61a–r]

Acknowledgements

We thank the Shiv Nadar Institution of Eminence for the research facilities, infrastructure, funding, and research assistantship for AV, AK, and Sourabh. We thank Prof. Ulrike Holzgrabe and Dr. Joshua Weinmann, University of Würzburg, for providing the compound for the preliminary crystallization experiments, Anton Parr Pvt. Ltd. for recording the VT-PXRD data, and Dr. Prathapa S. Jagannatha, Bruker India Scientific Private Limited, for assisting with the single-crystal X-ray diffraction data analysis.

References

1 T. Besara, P. Jain, N. S. Dalal, P. L. Kuhns, A. P. Reyes, H. W. Kroto and A. K. Cheetham, *Proc. Natl. Acad. Sci. U. S. A.*, 2011, **108**, 6828–6832.

2 P. Jain, N. S. Dalal, B. H. Toby, H. W. Kroto and A. K. Cheetham, *J. Am. Chem. Soc.*, 2008, **130**(32), 10450–10451.

3 W. M. W. Winters, C. Zhou, J. Hou, M. Diaz-Lopez, T. D. Bennett and Y. Yue, *Chem. Mater.*, 2024, **36**(17), 8400–8411.

4 Y.-Q. Wu, J.-Y. Zhang, X. He, Z.-X. Wang, H.-L. Cai and M.-X. Li, *Cryst. Growth Des.*, 2021, **21**(11), 6245–6253.

5 R. Pallach, J.-B. Weiss, K. Vollmari and S. Henke, *APL Mater.*, 2023, **11**, 041118.

6 W. Wei, W. Li, K. T. Butler, G. Feng, C. J. Howard, M. A. Carpenter, P. Lu, A. Walsh and A. K. Cheetham, *Angew. Chem., Int. Ed.*, 2018, **57**(29), 8932–8936.

7 M. Ptak, A. Kabanski, B. Dziuk, S. Balciunas, G. Usevicius, J. K. Zareba, J. Banys, M. Simenas, A. Sieradzki and D. Stefanska, *J. Mater. Chem. C*, 2024, **12**, 4663–4675.

8 D. Alloyeau, C. Ricolleau, C. Mottet, T. Oikawa, C. Langlois, Y. Le Bouar, N. Braidy and A. Loiseau, *Nat. Mater.*, 2009, **8**, 940–946.

9 J. Heo, D. D. Torres, P. Banerjee and P. K. Jain, *Nat. Commun.*, 2019, **10**, 1505.

10 Y. Miyazaki, T. Nakamoto, S. Ikeuchi, K. Saito, A. Inaba, M. Sorai, T. Tojo, T. Atake, G. S. Matouzenko, S. Zein and S. A. Borshch, *J. Phys. Chem. B*, 2007, **111**(43), 12508–12517.

11 M. Maczka, A. Pietraszko, B. Macalik and K. Hermanowicz, *Inorg. Chem.*, 2014, **53**(2), 787–794.

12 J. Berstein. *Polymorphism in Molecular Crystals*. Oxford University Press. 2020.

13 C. Brandel, Y. Cartigny, N. Couvrat, M. E. S. Eusebio, J. Canotilho, S. Petit and G. Coquerel, *Chem. Mater.*, 2015, **27**(18), 6360–6373.

14 V. K. Srirambhatla, R. Guo, D. M. Dawon, S. L. Price and A. L. Florence, *Cryst. Growth Des.*, 2020, **20**(3), 1800–1810.

15 R. Oketani, H. Takahashi, S. Clevers, A. Oyamada, I. Hisaki, G. Coquerel, K. Yamanaka and H. Tsue, *Cryst. Growth Des.*, 2022, **22**(4), 2230–2238.

16 J. S. O. Evans, *J. Chem. Soc., Dalton Trans.*, 1999, 3317–3326.

17 K. Takenaka, *Sci. Technol. Adv. Mater.*, 2012, **13**, 013001.

18 M. Azuma, W. T. Chen, H. Seki, M. Czapski, S. Olga, K. Oka, M. Mizumaki, T. Watanuki, N. Ishimatsu, N. Kawamura, S. Ishiwata, M. G. Tucker, Y. Shimakawa and J. P. Attfield, *Nat. Commun.*, 2011, **2**, 347.

19 S. E. Tallentire, F. Child, I. Fall, L. Vella-Zarb, I. R. Evans, M. G. Tucker, D. A. Keen, C. Wilson and J. S. Evans, *J. Am. Chem. Soc.*, 2013, **135**, 12849–12856.

20 A. L. Goodwin, M. Calleja, M. J. Conterio, M. T. Dove, J. S. O. Evans, D. A. Keen, L. Peters and M. G. Tucker, *Science*, 2008, **319**(5864), 794–797.

21 S. Sarkar and B. B. Iversen, *Angew. Chem., Int. Ed.*, 2025, **64**, e202503365.

22 A. L. Goodwin, K. W. Chapman and C. J. Kepert, *J. Am. Chem. Soc.*, 2005, **127**, 17980–17981.

23 M. K. Panda, T. Runčevski, S. C. Sahoo, A. A. Belik, K. N. Nath, R. E. Dinnebier and P. Naumov, *Nat. Commun.*, 2014, **5**, 4811.

24 Y. Wu, A. Kobayashi, G. J. Halder, V. K. Peterson, K. W. Chapman, N. Lock, P. D. Southon and C. J. Kepert, *Angew. Chem., Int. Ed.*, 2008, **47**, 8929–8932.

25 S. Henke, A. Schneemann and R. A. Fischer, *Adv. Funct. Mater.*, 2013, **23**, 5990–5996.

26 D. Das, T. Jacobs and L. J. Barbour, *Nat. Mater.*, 2010, **9**, 36–39.

27 S. Dutta and P. Munshi, *J. Phys. Chem. C*, 2020, **124**, 27413–27421.

28 S. Dutta, Vikas, V. Thangavel and P. Munshi, *ACS App. Electron. Mater.*, 2021, **3**(8), 3633–3640.

29 S. Hasebe, Y. Hagiwara, T. Ueno, T. Asahi and H. Koshima, *Chem. Sci.*, 2024, **15**, 1088–1097.

30 S. Dutta, L. Negi and P. Munshi, *Mater. Adv.*, 2024, **5**, 7495–7515.

31 H. Birkedal, D. Schwarzenbach and P. Pattison, *Angew. Chem., Int. Ed.*, 2002, **41**, 754–756.

32 H. Takahashi and R. Tamura, *CrystEngComm*, 2015, **17**, 8888–8896.

33 Vikas, L. Negi and P. Munshi., *Cryst. Growth Des.*, 2024, **24**(6), 2533–2541.

34 M. Berninger, C. Erk, A. Fuβ, J. Skaf, E. Al-Momani, I. Israel, M. Raschig, P. Guntzel., S. Samnick and U. Holzgrabe, *Eur. J. Med. Chem.*, 2018, **152**, 377–391.

35 J. Weinmann, L. Kirchner, M. Engstler, L. Meinel and U. Holzgrabe, *Eur. J. Med. Chem.*, 2023, **250**, 115176.

36 A. Kumar, J. Chauhan, K. D. Dubey, S. Sen and P. Munshi, *Mol. Pharmaceutics*, 2022, **19**(3), 1008–1018.

37 S. Dimitrovska-Lazova, M. Bukleski, P. Tzvetkov, M. Pecovska-Gjorgjevich, D. Kovacheva and S. Aleksovska, *Mater. Chem. Phys.*, 2022, **275**, 125240.

38 M. Szafrański and A. Katrusiak, *Phys. Rev. B*, 2000, **61**, 1026–1035.

39 K. K. Jha, S. Dutta, V. Kumar and P. Munshi, *CrystEngComm*, 2016, **18**, 8497–8505.

40 D. Dey, S. P. Thomas, M. A. Spackman and D. Chopra, *Chem. Commun.*, 2016, **52**, 2141–2144.

41 *APEX3, SAINT, and SADABS*, Bruker AXS, Inc., Madison, WI, USA, 2016.

42 G. M. Sheldrick, *SHELXTL v 2014/7*, https://shelx.uni-ac.gwdg.de/SHELX/index.php.

43 V. O. Dolomanov, L. J. Bourhis, R. J. Gildea, J. A. K. Howard and H. Puschmann, *J. Appl. Cryst.*, 2009, **42**, 339–341.

44 T. Rekis, A. Schönleber, L. Noohinejad, M. Tolkiehn, C. Paulmann and S. van Smaalen, *Cryst. Growth Des.*, 2021, **21**, 2324–2331.

45 S. Dey, S. Sasmal, S. Mondal, S. Kumar, R. Chowdhury, D. Sarkar, C. Malla Reddy, L. Peters, G. Roth and D. Haldar, *Acta Crystallogr., Sect. B:Struct. Sci.*, 2023, **B79**, 148–156.

46 C. P. Brock and J. D. Dunitz, *Chem. Mater.*, 1994, **6**(8), 1118–1127.

47 N. K. Nath and A. Nangia, *CrystEnggComm*, 2011, **13**, 47–51.

48 C. F. Macrae, I. Sovago, S. J. Cottrell, P. T. A. Gallek, P. McCabe, E. Pidcock, M. Platings, G. P. Shields, J. S. Stevens, M. Towler and P. A. Wood, *J. Appl. Cryst.*, 2020, **53**, 226–235.

49 J. Harada and K. Ogawa, *Chem. Soc. Rev.*, 2009, **38**, 2244–2252.

50 J. Harada and K. Ogawa, *J. Am. Chem. Soc.*, 2001, **123**(44), 10884–10888.

51 A. J. Cruz-Cabeza and J. Berstein, *Chem. Rev.*, 2014, **114**(4), 2170–2191.

52 G. Gupta, Y. Gupta, A. Kumar, R. Bhowal and P. Munshi, *Cryst. Growth Des.*, 2024, **24**(2), 646–656.

53 M. J. Turner, S. P. Thomas, M. W. Shi, D. Jayatilaka and M. A. Spackman, *Chem. Commun.*, 2015, **51**, 3735–3738.

54 P. R. Spackman, M. J. Turner, J. J. McKinnon, S. K. Wolff, D. J. Grimwood, D. Jayatilaka and M. A. Spackman, *J. Appl. Cryst.*, 2021, **54**, 1006–1011.

55 M. J. Frisch, G. W. Trucks, H. B. Schlegel, G. E. Scuseria, M. A. Robb, J. R. Cheeseman, G. Scalmani, V. Barone, B. Mennucci, G. A. Petersson *et al.*, *Gaussian 09, Revision E.01*, Gaussian, Inc., Wallingford, CT, 2009.

56 C. Lee, W. Yang and R. G. Parr, Development of the Colle-Salvetti Correlation-Energy Formula into a Functional of the Electron Density, *Phys. Rev.*, 1988, **B37**, 785–789.

57 A. Gavezzotti, *Z. Kristallogr. – Cryst. Mater.*, 2005, **220**, 499–510.

58 S. P. Thomas, P. R. Spackman, D. Jayatilaka and M. A. Spackman, *J. Chem. Theory Comput.*, 2018, **14**, 1614–1623.

59 M. J. Cliffe and A. L. Goodwin, *J. Appl. Cryst.*, 2012, **45**, 1321–1329.

60 L. Negi, A. Shrivastava and D. Das, *ChemComm*, 2018, **54**, 10675–10678.

61 (*a*) CCDC 2386800: Experimental Crystal Structure Determination, 2026, DOI: 10.5517/ccdc.csd.cc2l3nky; (*b*) CCDC 2386801: Experimental Crystal Structure Determination, 2026, DOI: 10.5517/ccdc.csd.cc2l3nlz; (*c*) CCDC 2386802: Experimental

Crystal Structure Determination, 2026, DOI: 10.5517/ccdc.csd.cc2l3nm0; (*d*) CCDC 2386803: Experimental Crystal Structure Determination, 2026, DOI: 10.5517/ccdc.csd.cc2l3nn1; (*e*) CCDC 2386804: Experimental Crystal Structure Determination, 2026, DOI: 10.5517/ccdc.csd.cc2l3np2; (*f*) CCDC 2386805: Experimental Crystal Structure Determination, 2026, DOI: 10.5517/ccdc.csd.cc2l3nq3; (*g*) CCDC 2386806: Experimental Crystal Structure Determination, 2026, DOI: 10.5517/ccdc.csd.cc2l3nr4; (*h*) CCDC 2386807 Experimental Crystal Structure Determination, 2026, DOI: 10.5517/ccdc.csd.cc2l3ns5; (*i*) CCDC 2386808: Experimental Crystal Structure Determination, 2026, DOI: 10.5517/ccdc.csd.cc2l3nt6; (*j*) CCDC 2386809: Experimental Crystal Structure Determination, 2026, DOI: 10.5517/ccdc.csd.cc2l3nv7; (*k*) CCDC 2386810: Experimental Crystal Structure Determination, 2026, DOI: 10.5517/ccdc.csd.cc2l3nw8; (*l*) CCDC 2386811: Experimental Crystal Structure Determination, 2026, DOI: 10.5517/ccdc.csd.cc2l3nx9; (*m*) CCDC 2386812: Experimental Crystal Structure Determination, 2026, DOI: 10.5517/ccdc.csd.cc2l3nyb; (*n*) CCDC 2386813: Experimental Crystal Structure Determination, 2026, DOI: 10.5517/ccdc.csd.cc2l3nzc; (*o*) CCDC 2386814: Experimental Crystal Structure Determination, 2026, DOI: 10.5517/ccdc.csd.cc2l3p0f; (*p*) CCDC 2386815: Experimental Crystal Structure Determination, 2026, DOI: 10.5517/ccdc.csd.cc2l3p1g; (*q*) CCDC 2386816: Experimental Crystal Structure Determination, 2026, DOI: 10.5517/ccdc.csd.cc2l3p2h; (*r*) CCDC 2386889: Experimental Crystal Structure Determination, 2026, DOI: 10.5517/ccdc.csd.cc2l3rfx.